


# Where is the Supervirial hot gas? I: A pilot study with sightlines to Galactic X-ray binaries

Armando Lara-DI<sup>1</sup>,  Yair Krongold<sup>1</sup>, Smita Mathur<sup>2,3</sup>, Manami Roy<sup>3</sup>, Rebecca L. McClain<sup>2</sup>, Sanskriti Das<sup>4</sup>, Anjali Gupta<sup>5</sup>

<sup>1</sup>*Instituto de Astronomía, Universidad Nacional Autónoma de México, 04510 Mexico City, Mexico*

<sup>2</sup>*Department of Astronomy, The Ohio State University, 140 West 18th Avenue, Columbus, OH 43210, USA*

<sup>3</sup>*Center for Cosmology and Astro-Particle Physics, The Ohio State University, 191 West Woodruff Avenue, Columbus, OH 43210, USA*

<sup>4</sup>*Kavli Institute for Particle Astrophysics & Cosmology, Stanford University, 452 Lomita Mall, Stanford, CA 94305, USA*

<sup>5</sup>*Columbus State Community College, 550 E Spring Street, Columbus, OH 43210, USA*

Accepted XXX. Received YYY; in original form ZZZ

## ABSTRACT

Hot,  $\log(T/K) \sim 7.5$ , gas was recently discovered in the Milky Way in extragalactic sightlines. In order to determine its location, here we present sightlines to Galactic X-ray binaries (XRBs) passing through the Interstellar Medium (ISM). In this pilot study we investigate absorption features of  $S_{XVI}$ ,  $Si_{XIV}$ , and  $Ne_{IX}$  in the spectra of three XRBs, namely 4U 1735-44, 4U 1820-30, and Cyg X-2, using Chandra High Energy Transmission Grating archival observations. We do not detect any of these lines. We determine the  $2\sigma$  upper limit for the equivalent widths of the undetected absorption lines and the column densities of the corresponding ions. We note that the  $2\sigma$  upper limits for  $S_{XVI} K\alpha$  and  $Si_{XIV} K\alpha$  are an order of magnitude smaller than those previously detected in the extragalactic sightlines. Our finding suggests that if any gas at  $\log(T/K) > 7$  is present in the Galactic ISM, it is unlikely to be ubiquitous. This is an important result because it implies that  $S_{XVI}$ ,  $Si_{XIV}$  and  $Ne_{IX}$  absorption detected in extragalactic sightlines is not from the ISM, but is likely from a hot gas phase in the extraplanar region beyond the ISM or in the extended CGM.

## Key words:

Galaxy: evolution – Galaxy: abundances – Galaxy: structure – Galaxy: halo – X-rays: ISM

## 1 INTRODUCTION

Spiral galaxies are characterized by a prominent disk populated with stars. Between the stars resides the Interstellar Medium (ISM), a complex multi-phase environment comprising a mixture of dust, molecules, and atoms (e.g., Rogantini et al. 2021 and references therein).

Studies of the Milky Way’s ISM have shown that it comprises of a wide range of gas phases, from neutral atomic and molecular hydrogen to heavier ionized elements such as  $Si_{II}$ ,  $Si_{III}$ ,  $Si_{IV}$ ,  $Ne_{IX}$ ,  $O_{VI}$ , and  $O_{VII}$  (e.g., Werk et al. 2019 and references therein; Rogantini et al. 2021). Energetic phenomena like stellar winds, supernova explosions, and interactions between binary star systems can both ionize and disperse the elements in the ISM.

Above and below the galactic disk, we find a much more diffuse and ionized medium called the Circumgalactic Medium (CGM) (see Mathur 2022 for a review). The CGM is defined as the gas extending beyond the galactic disk and inside the Galactic virial radius. Elements in different ionization states, such as  $O_{VI}$ ,  $O_{VII}$ ,  $O_{VIII}$ , and  $Ne_{IX}$  have been found in the CGM of the Milky Way (e.g., Gupta

et al. 2012; Mathur 2012; Tumlinson et al. 2017; Das et al. 2019; Bhattacharyya et al. 2023; Lara-DI et al. 2023).

Unlike the Galactic disk’s energetic processes explaining the observed ionized elements in the ISM, the CGM lacks a precise, direct mechanism for producing and ionizing the gas. Theoretical simulations show that the CGM is shock heated during the collapse of material in galaxy formation (see Crain & van de Voort 2023 and references therein). Numerical simulations have proposed that feedback processes from starbursts and active galactic nuclei expelled ionized metals from the disk into the CGM (e.g., Stinson et al. 2012), playing a significant role in shaping the CGM.

The Milky Way’s CGM is composed of two or three dominant phases: one at virial temperature ( $\log(T/K) \sim 6$ ) Gupta et al. 2012 and references therein, a hotter component at super-virial temperature ( $\log(T/K) \sim 7 - 7.5$ ; e.g., Das et al. 2019; Das et al. 2021; Gupta et al. 2023; Bhattacharyya et al. 2023), and a sub-virial component at  $\log(T/K) \sim 5.5$  (Das et al. 2021). The  $\log(T/K) \sim 6$  component has been known for over two decades, but the  $\log(T/K) \sim 7$  has been recently discovered in the last few years (Das et al. 2019).

In a recent study using stacked X-ray spectral observations towards tens of different extragalactic sightlines, Lara-DI et al. (2023) detected  $Si_{XIV} K\alpha$  and  $S_{XVI} K\alpha$  in the CGM of the Milky Way. These lines are associated with a gas phase with temperature  $\log(T/K) \sim$

\* E-mail: alara@astro.unam.mx

7.5. Gas at these temperatures is not predicted by the simulations of galaxy formation (e.g., [Stinson et al. 2012](#)), and its detection raises fundamental questions: Does this gas component arise from the CGM or the ISM of our Galaxy? What is the role of the Galactic CGM in the evolution of the Galaxy? What could be the origin of such supervirial gas, and how is this gas interacting with the Galaxy?

Building on our understanding of ionized gas in the Milky Way, in the present work we analyze Chandra’s High-Energy Transmission Grating (HETG) X-ray observations toward three Galactic X-ray Binaries (XRBs): 4U 1735-44, 4U 1820-30, and Cyg X-2. This is a pilot study; in future works we will present spectra from a large sample of XRBs. Our goal is to investigate  $\text{NeX}$ ,  $\text{SiXIV}$ , and  $\text{SXVI}$  absorption that has been previously detected in the extragalactic sightlines (e.g., [Das et al. 2019](#); [Das et al. 2021](#); [Lara-DI et al. 2023](#); [McClain et al. 2024](#); [Lara-DI et al. 2024](#); [Roy et al. 2024](#) in prep.) and determine whether the absorption occurs in the ISM of the Galaxy, or it is truly from extended regions beyond the ISM.

We structure this paper as follows. In Section 2, we present the data sample. In Section 3, we describe the data analysis. In Section 4, we present our results. In Section 5, we discuss their implications, and in Section 6 we present our conclusions.

## 2 DATA SAMPLE

We downloaded 23 (623.56 ks) archival Chandra ACIS-S HETG observations towards XRBs 4U 1735-44, 4U 1820-30, and Cyg X-2 (see Table 1). These particular sources are 3 of the 41 Galactic XRBs with high signal-to-noise ratio (S/N) ( $> 50$ ) in the Chandra HETG database. A larger XRB sample will be used in a future paper (in preparation). We reprocessed these observations using `chandra_repro` script with the Chandra Interactive Analysis of Observations<sup>1</sup> (CIAO) software (v4.13).

We stacked the observations using the `combine_grating_spectra` command in the CIAO software. The stacking was performed in order to get four stacked spectra for each XRB: one for the High Energy Gratings (HEG) continuous clocking readout mode (CC) observations, the second one for the HEG timed exposure readout mode (TE) observations, the third for the Medium Energy (MEG) CC observations, and the last one for the MEG TE observations. The resolving power ( $\lambda/\Delta\lambda$ ) for HEG is 1000 at 12.4 Å, while in MEG is 540 at this same wavelength. In Table 2 we show the S/N per resolution element (SNRE) for CC (column 3) and TE (column 4) at 4.729 Å. At this wavelength, corresponding to the rest-wavelength of  $\text{SXVI K}\alpha$ , the SNRE is  $> 20$ . We note that the CC mode observations have larger exposure times, resulting in better SNRE, compared to TE mode observations.

We note that CC mode observations in all three XRBs have a higher exposure time than TE. Additionally, in 5 out of the 6 MEG/HEG stacked observations, CC has a higher count rate than TE. Therefore, the signal-to-noise ratio is higher in CC mode observations than in TE.

In the spectral range 4 - 19 Å, TE observations can be affected by pileup when the sources are observed in a high flux state (e.g., [Rogantini et al. 2021](#)). Pileup occurs when multiple photons are detected as a single event, leading to a loss of information and energy spectral distortion. Narrow features, corresponding to specific energy lines, are less affected by pileup due to the lower likelihood of multiple photons coincidentally arriving at the exact energy levels needed for

these features. Consequently, narrow features are less influenced by pileup compared to broader features in the observed X-ray spectra, as also noted by [Rogantini et al. \(2021\)](#). Therefore, we analyze both the TE and CC spectra of all the three targets.

The closest Galactic sightline in this work to an extragalactic sightline where super-virial hot gas has been detected in absorption has an angular separation of 54.7 degrees. This corresponds to the angular distance between 4U 1820-30 and 1ES 1553+113 ([Das et al. 2019](#)). Given this large separation, we cannot directly comment on the location of the hot gas in any particular extragalactic sightline.

## 3 ANALYSIS

We used the software `XSPEC`<sup>2</sup> (v12.13.0) and  $\chi^2$  statistics to perform the spectral fitting of the CC MEG and HEG observations of the three XRBs, analyzing six spectra simultaneously. We did the same for the TE observations.

We constrained our modeling to the spectral region around  $\pm 0.25$  Å from the expected position of the rest-wavelength of each ionic transition of interest, i.e.,  $\text{SXVI K}\alpha$  ( $\lambda$  4.729 Å),  $\text{SiXIV K}\alpha$  ( $\lambda$  6.182 Å), and  $\text{NeX K}\alpha$  ( $\lambda$  12.134 Å).

To begin with, we fit the local continuum in these small ranges using a power-law (`pow`). The `pow` parameters between MEG and HEG of the same observation were set to be the same; however, if necessary, we used the `constant` parameter to account for any difference in the counts between the data. On the other hand, the `pow` of the three XRBs was allowed to be different. Additionally, if the spectra presented another feature to the one we were looking for, we added a Gaussian profile (`agauss`) to account for it.

Then, with a narrow Gaussian profile at the rest wavelength of  $\text{SXVI K}\alpha$ ,  $\text{SiXIV K}\alpha$ , and  $\text{NeX K}\alpha$  we modeled the possible presence of an absorption feature. We set the position of each Gaussian profile to the expected value of the line and let it vary  $\pm 0.012$  Å, corresponding to the resolution element of MEG and two times the resolution element of HEG. Finally, we fixed the line width to zero Å (since the lines are unresolved with the HETG resolution) and let the normalization vary. The line’s position and normalization were forced to be the same in all the six spectra of each XRB.

## 4 RESULTS

In the line of sight towards 4U 1735-44, 4U 1820-30, and Cyg X-2, we do not detect any absorption line at  $z \approx 0$  corresponding to  $\text{NeX}$ ,  $\text{SiXIV}$ , or  $\text{SXVI}$ . Since the fit statistically does not require any of these lines, we have determined the  $2\sigma$  upper limit for the equivalent width (EW) and ionic column density ( $N_{\text{ion}}$ ) of any undetected ISM absorption. Our results are shown in Table 3, which includes (1) the exposure mode, (2) the expected ionic transition, (3) the center of the undetected absorption line, (4) the  $2\sigma$  upper limit of the EW (mÅ), (5) the  $2\sigma$  upper limit of the  $N_{\text{ion}}$  calculated using the curve of growth, (6) the  $\chi^2/\text{d.o.f}$  statistics of the fit modeling the linear part of the local continuum, (7) and the  $\chi^2/\text{d.o.f}$  statistics of the fit when an absorption feature is considered in the spectra at the expected ionic transition (hereafter c+1).

In each absorption feature, the  $2\sigma$  upper limit of the EW is below 0.5 mÅ. We note that these values are consistently greater in TE than in CC data, consistent with the better S/N in the CC spectra.

We also performed the analysis separately on the individual spectra

<sup>1</sup> <https://asc.harvard.edu/ciao/>

<sup>2</sup> <https://heasarc.gsfc.nasa.gov/docs/software/heasoft/>

**Table 1.** ObsID List

Target (1)	Galactic Lon [deg] (2)	Galactic Lat [deg] (3)	Distance [kpc] (4)	Exp. Mode (5)	Exp. Time (ks) (6)	ObsIDs
4U 1735-44	346.053614	-6.993435	9.2 <sup>a</sup>	CC	47.12	6637, 6638
				TE	24.35	704
4U 1820-30	2.788145	-7.913689	6.4 <sup>b</sup>	CC	299.15	663, 6634, 7032, 22276, 22277, 24698, 25029
				TE	20.29	25030, 25031, 25032, 25033, 25037, 25038
Cyg X-2	87.32845	-11.316192	7.2 <sup>c</sup>	CC	189.38	8170, 8599, 10881
				TE	43.27	1102, 1016
TOTAL					623.56	

<sup>a</sup> van Paradijs & White 1995<sup>b</sup> Vacca et al. 1986<sup>c</sup> Orosz & Kuulkers 1999**Table 2.** Signal to Noise ratio (S/N) per resolution element (SNRE ; 23 mÅ for MEG, and 12 mÅ for HEG) at 4.729 Å in CC (column 3) and TE (column 4) spectra.

Target (1)	Grating (2)	CC (3)	TE (4)
4U 1735-44	HEG	29	21
	MEG	61	40
4U 1820-30	HEG	75	19
	MEG	162	43
Cyg X-2	HEG	115	33
	MEG	212	72

of each X-ray binary. We did not detect any lines, consistently with the results reported above. In Table 4, we show the  $2\sigma$  upper limit of the EW (mÅ) and  $N_{\text{ion}}$  for each sightline when we analyzed each spectrum separately. In Figure 1 we show MEG (CC) spectra around  $\text{NeX } K\alpha$ ,  $\text{Si}_{\text{XIV}} K\alpha$ , and  $\text{S}_{\text{XVI}} K\alpha$  toward each sightline, with the line upper limit superposed (red line). For comparison, we overplotted absorption lines stronger by a factor of 3 (dashed green line). These stronger features are not lost in the noise in most of the panels in Figure 1. In MEG, the resolution element is  $\Delta\lambda = 0.023 \text{ \AA}$ , while the pixel scale is  $0.01112 \text{ \AA}$  per pixel, resulting in approximately 2.06 pixels per resolution element. However, each channel in the MEG spectrum is separated by  $\Delta\lambda = 0.005 \text{ \AA}$ , leading to about 4.6 MEG channels per resolution element. Therefore, for visual purposes only, we have binned the spectra in Figure 1 by a factor of 5, corresponding to approximately 2 pixels. This is also consistent with the SNRE reported in Table 2.

## 5 DISCUSSION

Different studies have characterized a hot gas phase at  $\log(T/K) \sim 6$  in the ISM of the Milky Way (e.g., Rogantini et al. 2021). Consistently,  $\text{Ne}_{\text{IX}}$ , arising from this gas phase, has been detected towards the sightlines analyzed here (e.g., Pinto et al. 2013 for 4U 1735-44; Cackett et al. 2008 for 4U 1820-30; Yao et al. 2009 for Cyg X-2). On the other hand,  $\text{Ne}_{\text{X}}$ ,  $\text{Si}_{\text{XIV}}$ , and  $\text{S}_{\text{XVI}}$  are charge states tracing hotter gas. We do not detect these ions in the spectra of these XRBs. Furthermore, we are not aware of any detection of these charge states in the Galactic ISM in literature. This suggests that while gas at  $\log(T/K) \sim 6$  is commonly found in the ISM, hotter gas is not.

The  $2\sigma$  upper limits for the EW and  $N_{\text{ion}}$  of the undetected ISM absorption features at the rest-wavelength of  $\text{S}_{\text{XVI}} K\alpha$  and  $\text{Si}_{\text{XIV}} K\alpha$  are at least an order of magnitude smaller than those measured

in the extragalactic sightlines (e.g., Das et al. 2021; Lara-DI et al. 2023). Similarly, the  $2\sigma$  upper limits for  $N_{\text{ion}}$  of  $\text{Ne}_{\text{X}}$  are an order of magnitude smaller than the detection column densities in Das et al. (2019, 2021) and McClain et al. (2024). Therefore, the ISM contribution to the super-virial hot component detected in the extragalactic sightlines is negligible.

The above result is derived from only three XRB sightlines in this pilot study. In future works we will extend this to a large sample of XRBs to arrive at a firm conclusion. If the super-virial hot component is not in the ISM, as suggested here, it will have to be in regions beyond the ISM. It may be in the extra-planar region (e.g., Vijayan & Li 2021) or in the extended diffuse CGM. At this stage we cannot disentangle these two possibilities.

In order to determine whether we can detect the weak ISM lines from the hot gas ( $\log(T/K) \sim 7 - 7.5$ ), if any, with future observations, we simulated the XRISM spectra. We used the best fit model of the  $\text{Si}_{\text{XIV}}$  line from the Chandra HEG observation of Cyg X-2 in the CC mode. We assumed that the line strength is equal to the  $3\sigma$  upper limit observed with HEG (0.24 mÅ). After fitting the same model to the simulated XRISM data, we can detect the  $\text{Si}_{\text{XIV}} K\alpha$  line with  $3\sigma$  significance with a 60 ks exposure time. This is  $< 1/3$  exposure time of Chandra. If the actual line has smaller EW, the exposure time would be larger.

## 6 CONCLUSION

Our findings suggest that gas with super-virial temperatures is not commonly found in the Galactic ISM, and its contribution to the  $z = 0$  absorption detected in extragalactic sightlines is marginal, if any. The super-virial hot gas detected in the extragalactic sightlines is therefore likely to be present in the extraplanar region or in the extended CGM. In future works we plan on further disentangling the location of the hot gas.

## 7 ACKNOWLEDGMENTS

The authors of this work thank the anonymous referee for his/her valuable comments. L.D.I. acknowledges support from CONACYT through the PhD scholarship grant 760672. Y.K. acknowledges support from grant DGAPA PAPIIT 102023. S.M. is grateful for the grant provided by the National Aeronautics and Space Administration through Chandra Award Number AR0-21016X issued by the Chandra X-ray Center, which is operated by the Smithsonian Astrophysical Observatory for and on behalf of the National Aeronautics Space Administration under contract NAS8-03060. S.M. is

**Table 3.** Results. Here we present the  $2\sigma$  upper limits of absorption features observed in the positions of the ionic transitions. Spectra fitting was performed simultaneously for three XRB sightlines instead of stacking them. Results listed for CC are for MEG (CC) data shown in Fig. 1

Exposure Mode (1)	Ionic Transition (2)	Wavelength (Å) (3)	EW(mÅ) (4)	$N_{\text{ion}}$ (cm $^{-2}$ ) (5)	$\chi^2/\text{d.o.f}$ (6)	$\chi_{c+l}^2/\text{d.o.f}_{c+l}$ (7)
CC	Ne <sub>X</sub> ( $\lambda$ 12.134)	12.122	< 0.15	< $3.18 \times 10^{14}$	903.48/894	899.71/892
	Si <sub>XIV</sub> ( $\lambda$ 6.182)	6.176	< 0.05	< $4.09 \times 10^{14}$	1011.10/894	1010.84/892
	S <sub>XVI</sub> ( $\lambda$ 4.729)	4.717	< 0.07	< $9.78 \times 10^{14}$	1071.52/892	1065.64/894
TE	Ne <sub>X</sub> ( $\lambda$ 12.134)	12.125	< 0.38	< $8.07 \times 10^{14}$	813.88/894	809.22/892
	Si <sub>XIV</sub> ( $\lambda$ 6.182)	6.185	< 0.14	< $1.14 \times 10^{15}$	1025.32/894	1020.49/892
	S <sub>XVI</sub> ( $\lambda$ 4.729)	4.726	< 0.21	< $2.93 \times 10^{15}$	887.11/894	886.11/892

**Table 4.**  $2\sigma$  upper limit for the EW and  $N_{\text{ion}}$  for each sightline.

Target (1)	Mode (2)	Instrument (3)	Line (4)	$2\sigma$ EW [mÅ] (5)	$2\sigma N_{\text{ion}}$ [cm $^{-2}$ ] (6)
4U 1735-44	CC	MEG	Si <sub>XIV</sub>	<0.54	<4.42e+15
4U 1735-44	CC	MEG	S <sub>XVI</sub>	<0.78	<1.09e+16
4U 1735-44	CC	MEG	Ne <sub>X</sub>	<1.72	<3.65e+15
4U 1735-44	CC	HEG	S <sub>XVI</sub>	<0.86	<1.20e+16
4U 1735-44	CC	HEG	Si <sub>XIV</sub>	<0.55	<4.50e+15
4U 1735-44	CC	HEG	Ne <sub>X</sub>	<2.49	<5.28e+15
4U 1735-44	TE	HEG	S <sub>XVI</sub>	<1.29	<1.80e+16
4U 1735-44	TE	HEG	Si <sub>XIV</sub>	<0.83	<6.79e+15
4U 1735-44	TE	HEG	Ne <sub>X</sub>	<2.89	<6.13e+15
4U 1735-44	TE	MEG	S <sub>XVI</sub>	<1.19	<1.66e+16
4U 1735-44	TE	MEG	Si <sub>XIV</sub>	<0.88	<7.20e+15
4U 1735-44	TE	MEG	Ne <sub>X</sub>	<2.05	<4.35e+15
4U 1820-30	CC	MEG	S <sub>XVI</sub>	<0.29	<4.05e+15
4U 1820-30	CC	MEG	Si <sub>XIV</sub>	<0.19	<1.55e+15
4U 1820-30	CC	MEG	Ne <sub>X</sub>	<0.64	<1.36e+15
4U 1820-30	CC	HEG	S <sub>XVI</sub>	<0.28	<3.91e+15
4U 1820-30	CC	HEG	Si <sub>XIV</sub>	<0.22	<1.80e+15
4U 1820-30	CC	HEG	Ne <sub>X</sub>	<0.81	<1.72e+15
4U 1820-30	TE	MEG	S <sub>XVI</sub>	<1.12	<1.57e+16
4U 1820-30	TE	MEG	Si <sub>XIV</sub>	<0.81	<6.62e+15
4U 1820-30	TE	MEG	Ne <sub>X</sub>	<2.04	<4.33e+15
4U 1820-30	TE	HEG	S <sub>XVI</sub>	<1.13	<1.58e+16
4U 1820-30	TE	HEG	Si <sub>XIV</sub>	<0.81	<6.62e+15
4U 1820-30	TE	HEG	Ne <sub>X</sub>	<2.14	<4.54e+15
Cyg X-2	CC	MEG	S <sub>XVI</sub>	<0.22	<3.07e+15
Cyg X-2	CC	MEG	Si <sub>XIV</sub>	<0.14	<1.14e+15
Cyg X-2	CC	MEG	Ne <sub>X</sub>	<0.38	<8.07e+14
Cyg X-2	CC	HEG	S <sub>XVI</sub>	<0.18	<2.52e+15
Cyg X-2	CC	HEG	Si <sub>XIV</sub>	<0.16	<1.31e+15
Cyg X-2	CC	HEG	Ne <sub>X</sub>	<0.60	<1.27e+15
Cyg X-2	TE	MEG	S <sub>XVI</sub>	<0.64	<8.94e+15
Cyg X-2	TE	MEG	Si <sub>XIV</sub>	<0.53	<4.33e+15
Cyg X-2	TE	MEG	Ne <sub>X</sub>	<1.07	<2.27e+15
Cyg X-2	TE	HEG	S <sub>XVI</sub>	<0.61	<8.52e+15
Cyg X-2	TE	HEG	Si <sub>XIV</sub>	<0.47	<3.84e+15
Cyg X-2	TE	HEG	Ne <sub>X</sub>	<1.53	<3.25e+15

also grateful for the NASA ADAP grant 80NSSC22K1121. S.D. acknowledges support from the KIPAC Fellowship of Kavli Institute for Particle Astrophysics and Cosmology Stanford University.

#### DATA AVAILABILITY

All data used in this article are available online via the Chandra Data Archive: <https://cda.harvard.edu/chaser/>

#### REFERENCES

- Bhattacharyya J., Das S., Gupta A., Mathur S., Krongold Y., 2023, *ApJ*, **952**, 41
- Cackett E. M., Miller J. M., Raymond J., Homan J., van der Klis M., Méndez M., Steeghs D., Wijnands R., 2008, *The Astrophysical Journal*, **677**, 1233
- Crain R. A., van de Voort F., 2023, *ARA&A*, **61**, 473
- Das S., Mathur S., Nicastro F., Krongold Y., 2019, *ApJ*, **882**, L23
- Das S., Mathur S., Gupta A., Krongold Y., 2021, *ApJ*, **918**, 83
- Gupta A., Mathur S., Krongold Y., Nicastro F., Galeazzi M., 2012, *ApJ*, **756**, L8
- Gupta A., Mathur S., Kingsbury J., Das S., Krongold Y., 2023, *Nature As-*

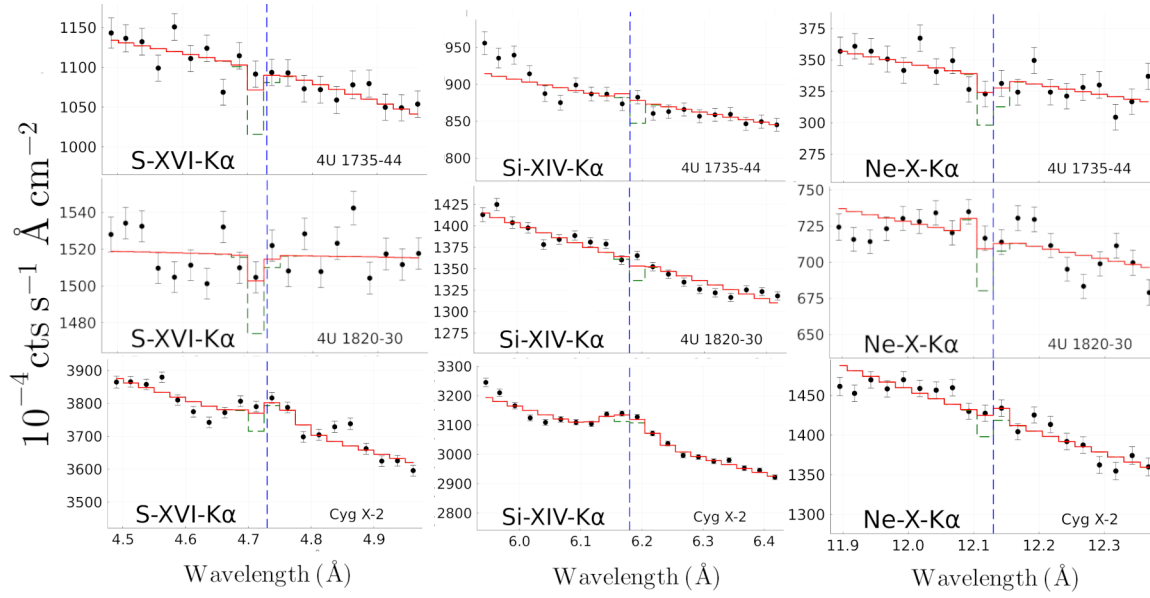


**Figure 1.** Here we display the model including the  $2\sigma$  upper limit of the normalization of absorption lines (red curve, Table 4) best-fitted to the MEG-CC data (black). We show for each sightline the position of  $\text{Ne}_X \text{K}\alpha$ ,  $\text{Si}_{XIV} \text{K}\alpha$ , and  $\text{S}_{XVI} \text{K}\alpha$  at  $z = 0$  (vertical blue dashed line). In dashed green are the absorption features superposed if they were three times stronger. Data points shown are binned by a factor of 5, and show resolution elements, not pixels or channels.

tronomy, 7, 799

Lara-DI A., Mathur S., Krongold Y., Das S., Gupta A., 2023, *The Astrophysical Journal*, 946, 55

Lara-DI A., Krongold Y., Mathur S., Das S., Gupta A., Segura Montero O., 2024, *Monthly Notices of the Royal Astronomical Society*, 531, 3034

Mathur S., 2012, *arXiv*, p. arXiv:1211.3137

Mathur S., 2022, Probing the Circumgalactic Medium with X-Ray Absorption Lines. Springer Nature Singapore, Singapore, pp 1–36, doi:10.1007/978-981-16-4544-0\_112-1, [https://doi.org/10.1007/978-981-16-4544-0\\_112-1](https://doi.org/10.1007/978-981-16-4544-0_112-1)

McClain R. L., Mathur S., Das S., Krongold Y., Gupta A., 2024, *MNRAS*, 527, 5093

Orosz J. A., Kuulkers E., 1999, *Monthly Notices of the Royal Astronomical Society*, 305, 132

Pinto C., Kaastra J. S., Costantini E., de Vries C., 2013, *A&A*, 551, A25

Rogantini D., Costantini E., Mehdipour M., Kuiper L., Ranalli P., Waters L. B. F. M., 2021, *A&A*, 645, A98

Stinson G. S., et al., 2012, *MNRAS*, 425, 1270

Tumlinson J., Peebles M. S., Werk J. K., 2017, *ARA&A*, 55, 389

Vacca W. D., Lewin W. H. G., van Paradijs J., 1986, *MNRAS*, 220, 339

Vijayan A., Li M., 2021, *Monthly Notices of the Royal Astronomical Society*, 510, 568

Werk J. K., et al., 2019, *The Astrophysical Journal*, 887, 89

Yao Y., Schulz N. S., Gu M. F., Nowak M. A., Canizares C. R., 2009, *The Astrophysical Journal*, 696, 1418

van Paradijs J., White N., 1995, *ApJ*, 447, L33

This paper has been typeset from a  $\text{\TeX}/\text{\LaTeX}$  file prepared by the author.